Spectroscopic failures in photometric redshift calibration: cosmological biases and survey requirements

Carlos E. Cunha[1,2⋆], Dragan Huterer[1], Huan Lin[3], Michael T. Busha[2,4], Risa H. Wechsler[2,5]

[1]*Department of Physics, University of Michigan, 450 Church St, Ann Arbor, MI 48109-1040*
[2]*Kavli Institute for Particle Astrophysics and Cosmology 452 Lomita Mall, Stanford University, Stanford, CA, 94305*
[3]*Center for Particle Astrophysics, Fermi National Accelerator Laboratory, Batavia, IL 60510*
[4]*Institute for Theoretical Physics, University of Zurich, 8057 Zurich, Switzerland*
[5]*Department of Physics, Stanford University, Stanford, CA, 94305,*
SLAC National Accelerator Laboratory, 2575 Sand Hill Rd., MS 29, Menlo Park, CA, 94025

16 July 2012

ABSTRACT

We use N-body-spectro-photometric simulations to investigate the impact of incompleteness and incorrect redshifts in spectroscopic surveys to photometric redshift training and calibration and the resulting effects on cosmological parameter estimation from weak lensing shear-shear correlations. The photometry of the simulations is modeled after the upcoming Dark Energy Survey and the spectroscopy is based on a low/intermediate resolution spectrograph with wavelength coverage of $5500\text{Å} < \lambda < 9500\text{Å}$. The principal systematic errors that such a spectroscopic follow-up encounters are incompleteness (inability to obtain spectroscopic redshifts for certain galaxies) and wrong redshifts. Encouragingly, we find that a neural network-based approach can effectively describe the spectroscopic incompleteness in terms of the galaxies' colors, so that the spectroscopic selection can be applied to the photometric sample. Hence, we find that spectroscopic incompleteness yields no appreciable biases to cosmology, although the statistical constraints degrade somewhat because the photometric survey has to be culled to match the spectroscopic selection. Unfortunately, wrong redshifts have a more severe impact: the cosmological biases are intolerable if more than a percent of the spectroscopic redshifts are incorrect. Moreover, we find that incorrect redshifts can also substantially degrade the accuracy of training set based photo-z estimators. The main problem is the difficulty of obtaining redshifts, either spectroscopically or photometrically, for objects at $z > 1.3$. We discuss several approaches for reducing the cosmological biases, in particular finding that photo-z error estimators can reduce biases appreciably.

1 INTRODUCTION

Large-scale structure surveys benefit enormously from the information about galaxy redshifts. The redshift information reveals the third spatial dimension of a galaxy survey, enabling a much more accurate mapping of the expansion and growth history of the Universe relative to the case when only angular information is available. Unfortunately, obtaining spectroscopic redshifts for all galaxies is typically impossible in wide-field imaging surveys due to the large number ($\sim 10^8$-10^9) of galaxies and the high cost of spectroscopy, especially for the high-redshift galaxies. To circumvent this problem, the current approach in the community is to estimate redshifts using photometric measurements, i.e. fluxes from a few broad band filters. These redshift estimates are known as photometric redshifts, or photo-zs, and are necessarily coarser than spectroscopic redshifts. Because of the intrinsically large errors, photo-zs typically cannot be used directly for cosmological analysis, unless the photo-z error distributions can be quantified precisely.

The standard approach to quantify, or calibrate, the photo-z error distributions is to use a small subsample of galaxies with known redshifts. As discussed in detail in Cunha et al. (2012), spectroscopic samples used to train photo-zs (cf. Sec. 4.2.2) need to be locally (in the space of observables) representative subsamples of the photometric samples. For calibration of the photo-z *error distributions*, however, the spectroscopic sample must be globally representative. More specifically, the ideal spectroscopic survey should satisfy the following properties:

• *Large area:* A spectroscopic survey needs to span a large area to beat down sample variance, and has to have tens of thousands of galaxies to beat down shot-noise in the photo-z error calibration (Cunha et al. 2012). In addition, the spectroscopic sample needs to be imaged under conditions that faithfully reproduce the variations in the full photometric sample (see e.g. Nakajima et al. 2012). Note that requirements might be alleviated with a correction to the individual galaxy redshift likelihoods (Bordoloi et al. 2010; Bordoloi et al. 2012). In the context of dark energy parameter constraints, however, a full analysis that goes beyond the overall redshift distribution and involves the full error matrix $P(z_s|z_p)$ is required (Bernstein & Huterer 2010; Hearin et al. 2010).

• *High completeness:* The spectroscopic survey needs to span the same range of redshifts, galaxy types, and other observational selection parameters as the photometric survey. When this is not possible, we say that the survey is *incomplete*. In that case, the photometric survey has to be culled to ensure both surveys have matching selections. Alternatively, the galaxies in the spectroscopic survey can be weighted so as to reproduce the statistical properties of the photometric sample. Achieving high completeness in faint spectroscopic surveys is a major challenge.

• *Few wrong redshifts:* We show in this paper that spectroscopic surveys need to have extremely accurate redshifts. As shown by many authors (e.g. Ma et al. 2006; Huterer et al. 2006; Amara & Refregier 2007; Abdalla et al. 2008; Ma & Bernstein 2008; Kitching et al. 2008; Hearin et al. 2010) the photo-z calibration requires exquisite knowledge of the photo-z error distribution. Errors in the spectroscopic redshifts impair the characterization of the photo-z errors and severely degrade our ability to extract cosmological constraints from photometric surveys.

For fixed observing resources, there is a conflict between accurate redshifts and completeness goals: as we stretch the observational limits (i.e. by observing very faint galaxies) to sample redshifts that would mimic the distribution of the photometric sample, we increase the fraction of incorrect spectroscopic redshifts. As we will show, redshift accuracy is more important for the upcoming surveys.

The purpose of this paper is to assess the impact of spectroscopic selection, i.e. completeness and accuracy, on the training and calibration of photometric redshifts and the resulting impact on cosmological constraints derived from weak lensing shear-shear correlations. To achieve this goal, we combine N-body, photometric and spectroscopic simulations patterned after the proposed characteristics of the Dark Energy Survey (DES) and expected spectroscopic follow-up. We then propagate the errors due to imperfect photo-z calibration on the cosmological parameter constraints inferred from the weak gravitational lensing power spectrum observations forecasted for the DES.

The paper is organized as follows. In Sec. 2 we provide a pedagogical introduction to the main issues driving completeness and accuracy of a spectroscopic sample. In Sec. 3 we briefly describe the simulated catalogs we use, leaving the details of the catalog generation to Appendix A. In Sec. 4 we give a step-by-step guide describing how we go from the simulated data to the cosmological constraints, detailing the methods used at each step. Results are presented in Sec. 5. We discuss the implications of our findings for spectroscopic survey design in Sec. 6 and present conclusions in Sec. 7.

2   BASICS OF LOW-RESOLUTION SPECTROSCOPY

In this section we provide a brief pedagogical overview of issues in spectroscopy, targeted to theorists.

2.1   Key parameters of spectroscopic surveys

Spectroscopic redshifts are often derived by cross-correlating a library of galaxy templates with observed (or simulated) spectra. For fixed observing conditions (and in the absence of instrumental systematic effects), three main items determine the quality of the estimated spectroscopic redshifts:

(i) *Spectral coverage:* The wavelength range covered by the spectrograph needs to bracket a few significant spectral features. As shown in the bottom plot of Fig. A1, for our simulation the coverage is roughly from 5500Å to 9500Å, with decreasing sensitivity at longer wavelengths.

(ii) *Integration time:* The faintest galaxies detectable by upcoming optical surveys can be a few orders of magnitude fainter than the atmospheric emission. Thus, significant integration times, as well as careful subtraction of the sky background, are needed to obtain secure redshift measurements.

(iii) *Cross-correlation templates:* Having an accurate and representative set of galaxy spectral distribution templates is important in deriving accurate redshifts and associated uncertainties. As we discuss in the next section, this is particularly important for early-type galaxies and galaxies at $z > 1.5$ (also known as the *redshift desert*) because of the lack of strong emission features in the spectrograph window.

2.2   Principal emission lines

The two main emission lines used in optical spectroscopy are the [OII] (singly-ionized oxygen) line at 3727Å and the $H\alpha$ (first transition in the Balmer series) line at 6563Å. The main absorption feature is the 4000Å break, caused by a confluence of absorption lines, particularly the H and K Calcium lines. In high-resolution spectroscopy, [OII] is the most important line because it is actually a doublet – a pair of closely spaced lines. High-resolution observations - e.g. with DEEP2 (Newman et al. 2012), or SDSS (York et al. 2000) - can distinguish the doublet and hence confidently identify [OII]. Low-resolution observations - e.g. as in the VVDS survey (Le Fèvre et al. 2005), which is the case we are simulating, rely on more than one feature. The limited spectral range of the instrument sets the regions of redshift space where one can confidently identify spectral features. In the case of VVDS, for example, there are roughly 5 different redshift regions:

• $z < 0.4$: The $H\alpha$ can be detected, but [OII] cannot. There is risk of confusing $H\alpha$ of a $z < 0.4$ galaxy for [OII] emission of a galaxy at $z > 0.8$. Fortunately, these galaxies are mostly brighter and thus the $H\alpha$ line combined with less prominent spectral features is often sufficient to estimate a redshift.

• $0.4 < z < 0.6$: Neither [OII] nor $H\alpha$ can be detected. Redshifts have to be estimated based on [OIII] and $H\beta$ lines.

• $0.6 < z < 0.9$: [OII] and other important lines ([OIII] - 5007Å, $H\beta$ - 4861Å) are detectable, but get progressively fainter towards higher redshift (due to increasing atmospheric noise and instrumental sensitivity).

• $0.9 < z < 1.5$: [OIII] and $H\beta$ are out of the instrument range, but [OII] is still detectable.

• $z > 1.5$ (the redshift desert): Only minor features in the spectra are available. Visual inspection to reduce incompleteness is essential in this range. Potential for wrong redshifts is increased because atmospheric emission lines can be mistakenly identified by the algorithm as real lines.

2.3   Additional systematics affecting the incompleteness

There are a few additional items contributing to the incompleteness that are not modeled in our simulations but that exist in real surveys:

• *Fiber collisions and slit overlaps*: If the angular separation between galaxies is too small, one may not simultaneously obtain
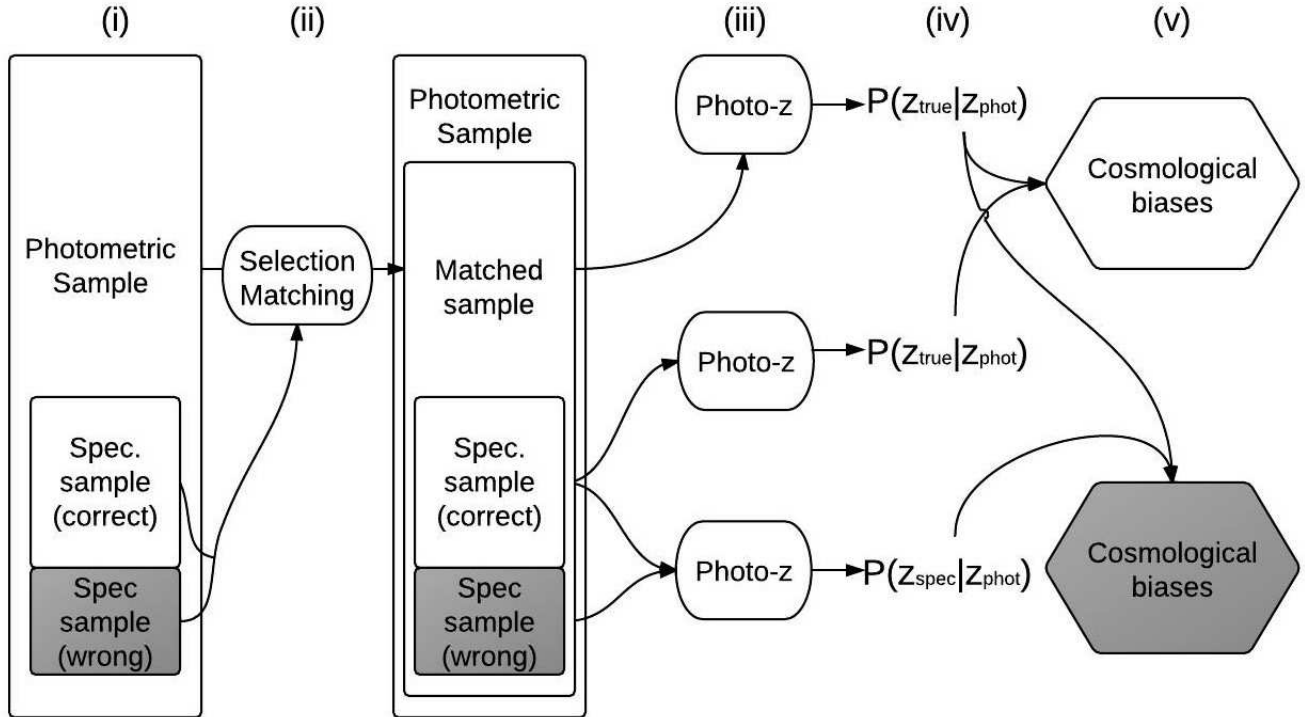
Figure 1. Flowchart describing our step-by-step procedure to go from the simulated observations to cosmological biases.

their spectra (without using a multiple pass strategy). Since clustering of galaxies is type dependent, one has to be careful that fiber collisions and slit overlaps do not introduce selection biases.

• *Optical distortions*: Geometric distortions due to the spectrograph optics may make extraction of spectra and subsequent measurement of redshifts more difficult near the edge of the instrument field of view.

• *CCD fringing*: Spatial and wavelength dependent variations in the pixel response in the red end of the spectrograph. Fringing hinders measurement of the spectra and redshifts of faint galaxies.

• *Stars and bright galaxies:* Light from nearby stars or bright galaxies can contaminate the spectra.

• *Cosmic rays*: Also can contaminate the spectra.

Issues such as stars, cosmic rays and edge effects will reduce the completeness, more or less randomly, resulting mostly in an increase in the shot noise, without galaxy type or redshift dependence.

3 SIMULATED DATA

We use cosmological simulations populated with galaxies and their photometric properties as described in Appendix A1. The photometric observations are patterned after the expected sensitivity of the Dark Energy Survey (DES) and Vista Hemisphere Surveys (VHS), with galaxies imaged in the grizYJHKs filters over 5100 sq. degrees. For simplicity, we only use the observations on *griz* bands because they are imaged for longer periods of time, and hence are useful for all our sample. The imaging in these bands is expected to reach 10σ magnitude limits of 25.2, 24.7, 24.0, and 23.5 in *g,r,i* and *z*.

For computational efficiency, we select a subsample of ap-

proximately 1.3 million galaxies, hereafter our *photometric sample*, from the total 1 billion galaxies present in the simulation. We apply the same quality cuts as in Cunha et al. (2012), i.e. keep galaxies with $i < 24$ and at least 5σ detection in *grz*. This selection reduces our photometric sample to 726824 galaxies.

Of this photometric sample, we randomly target a subset of 181892 galaxies, hereafter the *spectroscopic sample* or *training set*, for the spectroscopic analysis. The generation of simulated spectra for this subsample is described in the Appendix A2.

4 FROM THE REDSHIFTS TO COSMOLOGY

In this section, we describe the step-by-step procedure we used for converting the simulated observations into cosmological constraints. The flowchart in Fig. 1 gives a pictorial version of the explanation below.

(i) The first step is to estimate spectroscopic redshifts for the sample for which we have spectra. We use the `rvsao.xcsao` spectral analyzer algorithm described in Sec. 4.1. Not all spectra yield redshifts, and only the redshifts above certain confidence are kept. Even so, a fraction of the spectroscopic redshifts is incorrect.

(ii) The spectroscopic sample can only be used for calibration of the photo-z error distributions if it is a representative subsample of the photometric sample. Hence, we statistically match spectroscopic and photometric selection in one of two ways: by applying the spectroscopic selection to the photometric sample with neural networks (cf. Sec. 5.3), or by weighting the photometric sample so that its statistical properties match those of the spectroscopic sample (cf. Sec. 5.4).

(iii) Next, we calculate photo-zs for the both spectroscopic and photometric samples, cf. Sec. 4.2.

(iv) After the matching, we can calculate the photo-z error matrices required for cosmological analysis.

(v) Finally, we estimate fiducial constraints and biases in the cosmological parameters forecasted for the DES-type weak gravitational lensing survey. We break up the tests in two parts. In the first case, shown as the transparent hexagon in the flowchart, we only test the impact of the selection matching, by using only the correct value for redshifts. In the second case (gray hexagon), we use the actual value of the spectroscopic redshifts - thereby including the small fraction of wrong redshifts.

4.1   Analyzing 1-D spectra

Simulating spectroscopic redshift estimation is challenging because real spectroscopic surveys rely heavily on visual inspection. For our forecasts, visual inspection of thousands of spectra would be out of the question. Instead, we adopt a more reasonable strategy and apply an automated pipeline to all 1-D spectra. We use the publicly available rvsao IRAF external package version 2.7.8 (Kurtz & Mink 1998). We run the cross-correlation tool xcsao on our simulated spectra. The algorithm performs a Fourier cross-correlation between the "observed" (simulated) spectra and a user-defined library of template spectra. We obtain the template library used in the cross-correlation from the simulation itself. For the first pass, we pick 6 templates chosen to mimic the 6 galaxy templates used in the cross-correlation analysis of the SDSS spectroscopic pipeline[1]. Using templates from the simulation instead of the original SDSS templates improved the number of correct redshifts by 10%. The limitation of the SDSS template basis is that it was chosen for low redshift spectroscopy, and is not sufficient for redshifts greater than 1 or so. In the second pass, we added three templates from the simulations picked as the brightest templates above redshift 1.4 for which the cross-correlation coefficient — the R statistic described below — was less than 2.5. The additional templates doubled the number of correct redshifts above 1.4.

The cross-correlation analysis can be refined around certain wavelengths by giving it an initial redshift guess (by setting the parameter czguess) to start the search. We perform the analysis five times with: no guess, czguess = 0.4, czguess = 0.8, czguess = 1.2 and czguess=1.6. We then choose which redshift estimate to keep based on the value of the R statistic, output by the pipeline. The R statistic, introduced by Tonry & Davis (1979) (cf. Eq. 23 of that work), is a measure of the strength of the cross-correlation given by the ratio of the height of the assumed true peak in the correlation to the average height of spurious peaks. R varies from 1 to several hundred in our simulation, and as we show later, $R > 6$ corresponds to $> 99\%$ correct redshifts.

We have performed our analysis for a number of settings of the spectroscopic pipeline, but only show results for three main cases, defined as follows:

- *Fiducial Pipeline:* $z_{\rm spec}$s estimated using the 6+3=9 templates and the five redshift guesses described above. Yields the highest completeness for $z > 1.4$.
- *Comb2 Pipeline:* $z_{\rm spec}$s estimated using the 6+3=9 templates and only running xcsao twice, with czguess = 0.4 and czguess = 0.8. Yields the highest overall completeness, but the lowest completeness at low and high redshift.

- *Original Pipeline:* $z_{\rm spec}$s estimated using the 6 original templates and only four redshift guesses: czguess = none, 0.4, 0.8 and 1.2.

4.2   Photometric redshifts

There exists a cornucopia of publicly available photometric redshift estimation algorithms. For recent reviews and comparison of methods see e.g. Hildebrandt et al. (2010); Abdalla et al. (2011). We consider two different photo-z algorithms that broadly span the space of possibilities. We use a basic template-fitting code without any priors, and a training-set fitting method, which we briefly describe below.

4.2.1   Template-fitting redshift estimators

Template-fitting estimators derive photometric redshift estimates by comparing the observed colors of galaxies to colors predicted from a library of galaxy spectral energy distributions. We use the publicly available *LePhare* photo-z code[2] (Arnouts et al. 1999; Ilbert et al. 2006) as our template-fitting estimator. We chose the extended CWW template library (Coleman et al. 1980) because it yielded the best photo-zs for our simulation.

We note that a variety of public template-fitting codes are available (e.g. Coe et al. 2006; Feldmann et al. 2006), and each includes many options of template libraries, extinction laws, priors, etc. For a discussion on propagation of template-fitting uncertainties to redshift uncertainties see Abrahamse et al. (2011). As in Cunha et al. (2012), the photo-z quality does not significantly affect the results shown, hence we find no justification for an extensive exploration of all template-fitting possibilities.

4.2.2   Training-set redshift estimators

The basic setup of training-set based redshift estimators is to use a sample with known spectroscopic redshifts to estimate the free parameters of a function relating the observables (in our case the magnitudes of the galaxies) to the redshifts. After the best-fit free parameters have been determined, the function can be applied to the data for which no spectroscopic redshifts are available, known as the photometric sample. For this paper, we use an artificial neural network as our training set method, and we leave the details to Appendix B.

4.3   Effect on the Cosmological Parameters

To assess the impact of the spectroscopic failures on the cosmological parameters, we closely follow the formalism used in our previous work on the impact of sample variance to photo-z calibration (Cunha et al. 2012). We consider a weak lensing survey, and for simplicity only study the shear-shear correlations. The observable quantity we consider is the convergence power spectrum

$$C_{ij}^{\kappa}(\ell) = P_{ij}^{\kappa}(\ell) + \delta_{ij}\frac{\langle\gamma_{\rm int}^2\rangle}{\bar{n}_i}, \tag{1}$$
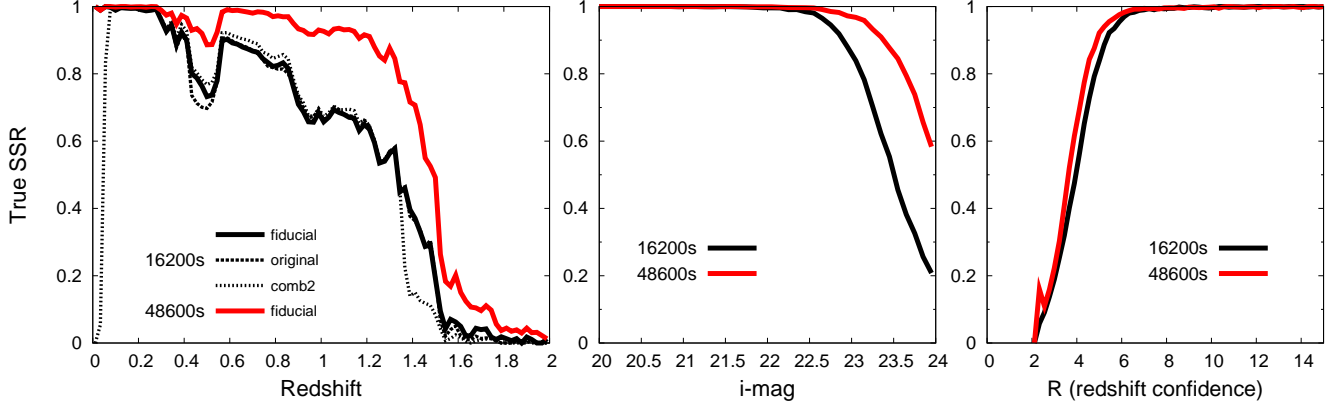
Figure 2. Left panel: True spectroscopic success rate (SSR_T), defined as fraction of correct redshifts, as a function of true redshift. Central panel: SSR_T as a function of observed i-band magnitude. Right panel: SSR_T as a function the cross-correlation strength statistic R, which is a measure of the redshift confidence. The black lines assume 16200 secs of integration time and the red (gray) lines assume 48600 secs. The solid, dashed and dotted lines correspond to different settings of the spectroscopic pipeline, described in Sec. 4.1.

where $\langle\gamma_{\rm int}^2\rangle^{1/2}$ is the rms intrinsic ellipticity in each component, $\bar{n}_i$ is the average number of galaxies in the ith redshift bin per steradian, and ℓ is the multipole that corresponds to structures subtending the angle $\theta = 180°/\ell$. For simplicity, we drop the superscripts κ below. We take $\langle\gamma_{\rm int}^2\rangle^{1/2} = 0.26$.

We follow the formalism of Bernstein & Huterer (2010) (hereafter BH10), where the photometric redshift errors are algebraically propagated into the biases in the shear power spectra. These biases in the shear spectra can then be straightforwardly propagated into the biases in the cosmological parameters. We now review briefly this approach.

Let us assume a survey with the (true) distribution of source galaxies in redshift $n_t(z)$, divided into B bins in redshift. Let us define the following terms

- Leakage $P(z_p|z_t)$ (or l_{tp} in BH10 terminology): fraction of objects from a given true redshift bin that are placed into an incorrect (non-corresponding) photometric bin.
- Contamination $P(z_t|z_p)$ (or c_{tp} in BH10 terminology): fraction of galaxies in a given photometric bin that come from a non-corresponding true-redshift bin.

When specified for each tomographic bin, these two quantities contain the same information. Note in particular that the two quantities satisfy the integrability conditions

$$\int P(z_p|z_t)dz_p \equiv \sum_p l_{tp} = 1 \qquad (2)$$

$$\int P(z_t|z_p)dz_t \equiv \sum_t c_{tp} = 1. \qquad (3)$$

A fraction l_{tp} of galaxies in some true-redshift bin n_t "leak" into some photo-z bin n_p, so that l_{tp} is the fractional perturbation in the true-redshift bin, while the contamination c_{tp} is the fractional perturbation in the photometric bin. The two quantities can be related via

$$c_{tp} = \frac{N_t}{N_p} l_{tp} \qquad (4)$$

where N_t and N_p are the absolute galaxy numbers in the true and photometric redshift bins, respectively. Then,

$$n_t \rightarrow n_t \qquad (5)$$

$$n_p \rightarrow (1 - c_{tp})\, n_p + c_{tp}\, n_t \qquad (6)$$

and the photometric bin normalized number density is affected (i.e. biased) by photo-z catastrophic errors. The effect on the cross power spectra is then

$$
\begin{aligned}
C_{pp} &\rightarrow (1-c_{tp})^2 C_{pp} + 2c_{tp}(1-c_{tp})C_{tp} + c_{tp}^2 C_{tt} \\
C_{mp} &\rightarrow (1-c_{tp})C_{mp} + c_{tp}\, C_{mt} \qquad (m < p) \\
C_{pn} &\rightarrow (1-c_{tp})C_{pn} + c_{tp}\, C_{tn} \qquad (p < n) \\
C_{mn} &\rightarrow C_{mn} \qquad \text{(otherwise)}
\end{aligned}
\qquad (7)
$$

(since the cross power spectra are symmetrical with respect to the interchange of indices, we only consider the biases in power spectra C_{ij} with $i \leqslant j$). Note that these equations are exact for a fixed contamination coefficient c_{tp}.

The bias in the observable power spectra is the rhs-lhs difference in the above equations[3]. The cumulative result due to all contaminations in the survey (or, $P(z_t|z_p)$ values for each z_t and z_p binned value) can be obtained by the appropriate sum

$$
\begin{aligned}
\delta C_{pp} &= \sum_t (-2c_{tp} + c_{tp}^2)C_{pp} + 2c_{tp}(1-c_{tp})C_{tp} + c_{tp}^2 C_{tt} \\
\delta C_{mp} &= \sum_t (-c_{tp}C_{mp} + c_{tp}\, C_{mt}) \qquad (8) \\
\delta C_{pn} &= \sum_t (-c_{tp}C_{pn} + c_{tp}\, C_{tn})
\end{aligned}
$$

for each pair of indices (m, p), where the second and third line assume $m < p$ and $p < n$, respectively.

The bias in cosmological parameters is given by using the standard linearized formula (Knox et al. 1998; Huterer & Turner 2001), summing over each pair of contaminations (t, p)

$$\delta p_i \approx \sum_j (F^{-1})_{ij} \sum_{\alpha\beta} \frac{\partial \bar{C}_\alpha}{\partial p_j}(\text{Cov}^{-1})_{\alpha\beta}\, \delta C_\beta, \qquad (9)$$

where F is the Fisher matrix and **Cov** is the covariance of shear power spectra (see just below for definitions). This formula is accurate when the biases are 'small', that is, when the biases in the

---

[3] We have checked that the quadratic terms in c_{tp} are unimportant, but we include them in any case.

cosmological parameters are much smaller than statistical errors in them, or $\delta p_i \ll (F^{-1})_{ii}^{1/2}$. Here i and j label cosmological parameters, and α and β each denote a *pair* of tomographic bins, i.e. $\alpha, \beta = 1, 2, \ldots, B(B+1)/2$, where recall B is the number of tomographic redshift bins. To connect to the C_{mn} notation in Eq. (7), for example, we have $\beta = mB + n$.

We calculate the Fisher matrix F assuming perfect redshifts, and following the procedure used in many other papers (e.g. Huterer & Linder 2007). The weak lensing Fisher matrix is then given by

$$F_{ij}^{\mathrm{WL}} = \sum_\ell \frac{\partial \mathbf{C}}{\partial p_i} \mathbf{Cov}^{-1} \frac{\partial \mathbf{C}}{\partial p_j}, \qquad (10)$$

where p_i are the cosmological parameters and $\mathbf{Cov}^{-1}$ is the inverse of the covariance matrix between the observed power spectra whose elements are given by

$$\mathrm{Cov}\left[C_{ij}(\ell), C_{kl}(\ell')\right] = \frac{\delta_{\ell\ell'}}{(2\ell+1) f_{\mathrm{sky}} \Delta\ell} \times \qquad (11)$$
$$[C_{ik}(\ell)C_{jl}(\ell) + C_{il}(\ell)C_{jk}(\ell)].$$

The fiducial weak lensing survey corresponds to expectations from the Dark Energy Survey, and assumes 5000 square degrees (corresponding to $f_{\mathrm{sky}} \simeq 0.12$) with tomographic measurements in $B = 20$ uniformly wide redshift bins extending out to $z_{\mathrm{max}} = 2.0$. The effective source galaxy density is 12 galaxies per square arcminute, while the maximum multipole considered in the convergence power spectrum is $\ell_{\mathrm{max}} = 1500$. The radial distribution of galaxies, required to determine tomographic normalized number densities n_i in Eq. (1), is determined from the simulations and shown in Fig. 4.

We consider a standard set of six cosmological parameters with the following fiducial values: matter density relative to critical $\Omega_M = 0.25$, equation of state parameter $w = -1$, physical baryon fraction $\Omega_B h^2 = 0.023$, physical matter fraction $\Omega_M h^2 = 0.1225$ (corresponding to the scaled Hubble constant $h = 0.7$), spectral index $n = 0.96$, and amplitude of the matter power spectrum $\ln A$ where $A = 2.3 \times 10^{-9}$ (corresponding to $\sigma_8 = 0.8$). Finally, we add the information expected from the Planck survey given by the Planck Fisher matrix (W. Hu, private communication). The total Fisher matrix we use is thus

$$F = F^{\mathrm{WL}} + F^{\mathrm{Planck}}. \qquad (12)$$

The fiducial constraint on the equation of state of dark energy assuming perfect knowledge of photometric redshifts is $\sigma(w) = 0.055$.

Our goal is to estimate the biases in the cosmological parameters due to imperfect knowledge of the photometric redshifts. In particular, the relevant photo-z error will be the difference between the inferred $P(z_s|z_p)$ distribution for the calibration (or, training) set – using spectroscopic redshifts as a proxy for the true redshifts – and the $P(z_t|z_p)$ distribution for the actual survey. Therefore, we define

$$\delta C_\beta = C_\beta^{\mathrm{train}} - C_\beta^{\mathrm{phot}} \qquad (13)$$
$$= \delta C_\beta^{\mathrm{train}} - \delta C_\beta^{\mathrm{phot}} \qquad (14)$$

where the second line trivially follows given that the true, underlying power spectra are the same for the training and photometric galaxies. All of the shear power spectra biases δC can straightforwardly be evaluated from Eq. (8) by using the contamination coefficients for the training and photometric samples, respectively.

Therefore, the effective error in the power spectra is equal to the difference in the biases of the training set (our *estimates* of the biases in the observable quantities) and the photometric set (the actual biases in the observables).

5 RESULTS

5.1 Spectroscopic success rate

The spectroscopic analysis for the fiducial simulation parameters (16200 secs integration; 9 templates; no manual correction of spectra) yields about 74% correct spectroscopic redshifts (defined as redshifts for which $|z_{\mathrm{spec}} - z_{\mathrm{true}}| < 0.01$). In a real survey, one can only choose redshifts based on some quality flag, which is the cross-correlation R statistic (described in Sec. 4.1) in our case. We thus define two success metrics:

• *True spectroscopic success rate (*$\mathrm{SSR_T}$*)*: the fraction of galaxies with correct redshifts.
• *Observed SSR (*$\mathrm{SSR_O}$*)*: the fraction of galaxies with R greater than a certain value. Unless stated otherwise, we set the value to 6.0.

In Fig. 2, we show the true SSR as a function of true redshift (left panel), observed i-band magnitude (center panel) and cross-correlation strength (right panel). The left panel shows that the $\mathrm{SSR_T}$ generally worsens with higher redshift, and the 'hiccups' in the curves are directly caused by different spectral lines which enter and leave the observed spectral range, as discussed in Sec. 2. The central panel shows the expected result that the spectroscopic success rate plunges beyond certain depth. Finally, the right panel shows that the true SSR increases monotonically with cross-correlation statistic R, showing that we can use R to select an accurate redshift sample with high confidence.

In Fig. 3 we show the true and observed SSRs as a function of i-magnitude and r–i color. The top panel shows that virtually all the incorrect redshifts are at the faint end of the color-magnitude diagram, with slight color dependence. In particular, at the bluest end (r–$i \sim 0$) we see a region of low SSR extending to $i \sim 22$. This is typically caused by the lack of an appropriate template to describe certain galaxy populations.

The *observed* SSR, shown in the bottom panel of Fig. 3, shows a more pronounced color variation. We can see that the bluer colors, corresponding to late spectral types, which have significant emission features, yields highest $\mathrm{SSR_O}$. Conversely, the redder colors have the lowest $\mathrm{SSR_O}$. As mentioned previously, early type galaxies have virtually no emission lines, and hence are identified by absorption features. Intermediate types can have weak emission lines, but usually have weaker absorption features as well, which makes it difficult to determine a spectroscopic redshift for them.

Because of our stringent choice of cut, the sample with $R > 6.0$ contains a fraction 0.53 of the total galaxies and has 99.6% correct spectroscopic redshifts. For comparison, if we define samples by the cuts $R > 5.0$ and $R > 4.0$ these would contain a fraction of 0.60 and 0.73 of total galaxies with 98.6% and 93.2% correct redshifts, respectively. Faint, intermediate-type galaxy spectra yield the majority of the incorrect redshifts that escape the R selection.

In the top panel of Fig. 4 we show the effect of applying quality cuts based on the statistic R to the true redshift distribution. More stringent (higher R) cuts preferentially remove galaxies from regions where less significant spectroscopic features fall inside the spectrograph window (as explained in Sec. 2). The bottom panel
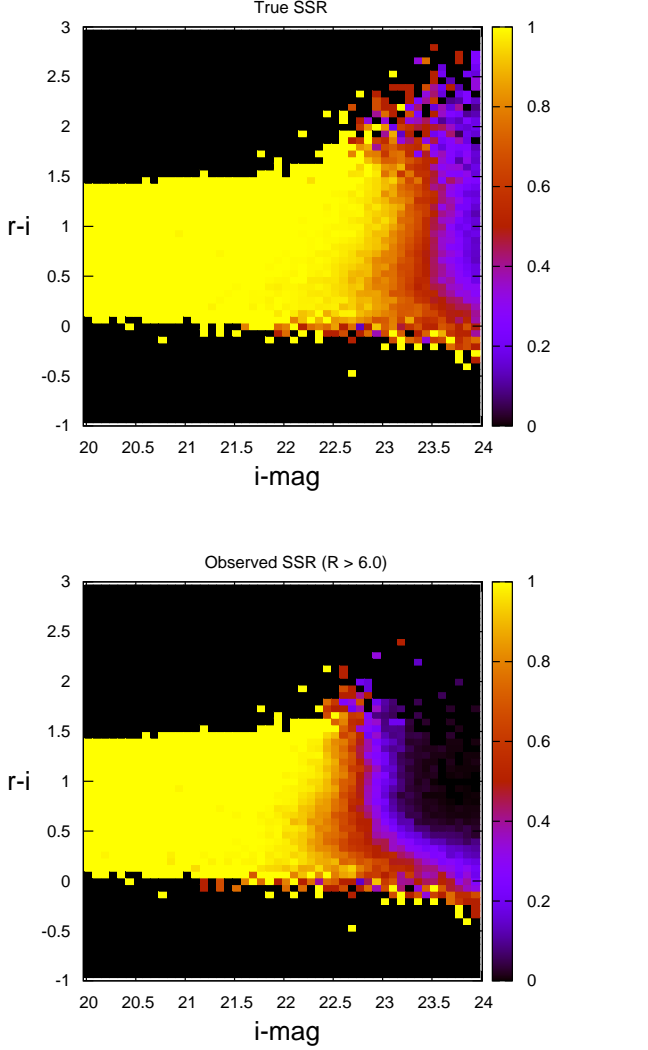
Figure 3. Top panel: True spectroscopic success rate (SSR$_T$), defined as fraction of correct redshifts as a function of true redshift. Bottom panel: Observed SSR (SSR$_O$), defined as fraction of galaxies with correlation $R > 6.0$. Both results assume the Fiducial pipeline settings (cf. Sec. 4.1) of 16200 secs of integration time with the 3 additional templates.

shows that the less stringent cuts allow for a higher fraction of incorrect redshifts, which have a visible impact in the redshift distribution even though 93.2% of the redshifts are correct.

5.2 Where do the wrong redshifts go?

We show the spectroscopic leakage matrices ($P(z_{\mathrm{spec}}|z_{\mathrm{true}})$) for several cuts in the R statistic for our Fiducial pipeline scenario in Fig. 5. The spectroscopic redshift errors, which correspond to any departures from the $z_{\mathrm{spec}} = z_{\mathrm{true}}$ (diagonal) line, clearly make interesting and definite patterns:

• *Atmospheric line confusion:* Horizontal features in Fig. 5, when many different values of z_{true} are misinterpreted as a single z_{spec}, correspond to cases where residuals from subtraction of atmospheric lines are confused with actual features in the galaxy spectrum.
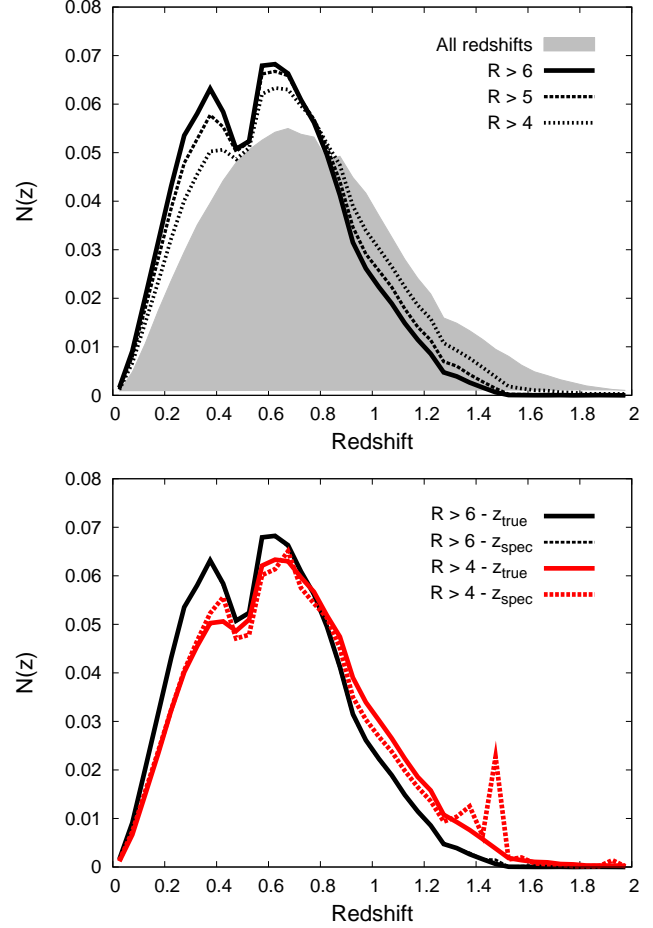
Figure 4. Top panel: Distributions of true redshift for all galaxies (shaded area), galaxies with $R > 6$ (solid line), galaxies with $R > 5$ (dashed line) and galaxies with $R > 4$ (dotted line). Bottom panel: Distribution of true redshift (solid lines) and spectroscopic redshift (dashed lines) for the $R > 6$ sample (black) and the $R > 4$ sample (red - gray).

• *Galaxy line misidentification:* Diagonal lines in Fig. 5 (excepting the $z_{\mathrm{spec}} = z_{\mathrm{true}}$ diagonal, of course) correspond to the cases where the pipeline misidentifies lines of the galaxy itself due to limited spectroscopic coverage and S/N (cf. Sec. 2.2). For example, the diagonal trend from $(z_{\mathrm{true}}, z_{\mathrm{spec}}) = (0, 0.8)$ to about $(0.7, 2.0)$ corresponds to the pipeline classifying Hα emission lines as [OII] lines. A corresponding feature due to [OII] being incorrectly classified as Hα can be seen starting at $(0.8, 0)$ in the plots. Galaxy line misidentification seems to be a much smaller issue than atmospheric line confusion for our simulation.

The exact distribution of the wrong redshifts depends on the noise levels assumed and details of the spectroscopic analysis. As described in Appendix A2, we assumed a constant mean atmospheric emission and absorption, but in reality the observing conditions vary. The distribution of wrong redshifts also depends on details of the spectroscopic analysis. In Fig. 6 we show the $P(z_{\mathrm{spec}}|z_{\mathrm{true}})$ matrix for the Original pipeline, described in Sec. 4.1, which only uses the original 6 spectral templates (but not the 3 templates added to increase completeness for $z > 1.4$.) In addition, it does not use the `czguess=1.6` results, which have the effect of increasing the probability that the pipeline will assign a high redshift to a galaxy. The Original pipeline is not optimized in any way towards high-z completeness, and as a result it finds no spectro-
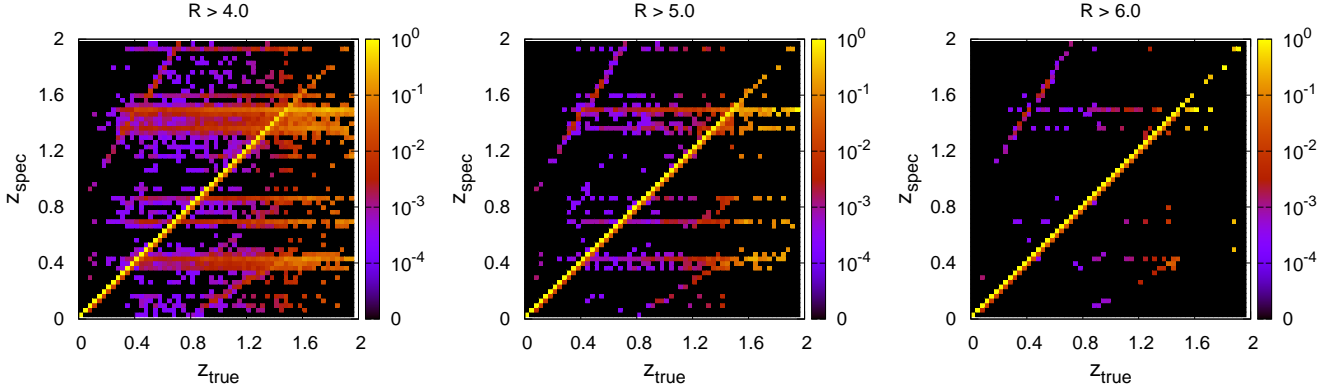
Figure 5. Leakage matrices ($P(z_{\rm spec}|z_{\rm true})$) for the training sets selected by the cuts $R > 4.0$ (left panel), $R > 5.0$ (center panel), and $R > 6.0$ (right panel). The spectroscopic redshifts were calculated using 16,200 secs exposures with the full set of 9 templates in the spectroscopic pipeline, corresponding to our Fiducial pipeline.

scopic redshifts above $z = 1.6$. Conversely, the Fiducial pipeline (cf. right plot in Fig. 5), does find some redshifts above $z = 1.6$, but at the cost of increasing the number of objects being incorrectly assigned very high values of spectroscopic redshifts and the number of objects at high redshifts being assigned very low redshifts. As we discuss in Sec. 5.3.2, the Original pipeline yields a bias in w a factor of two smaller than the Fiducial pipeline.

There are two points to take from this section. First, wrong spectroscopic redshifts occupy preferred regions of the ($z_{\rm true}$, $z_{\rm spec}$) plane. Since the exact redshift error distribution depends on the details of the spectroscopic analysis and observing conditions, it is challenging to accurately predict the spectroscopic redshift errors in real surveys. Hence, our conclusions concerning the impact of wrong redshift are necessarily only rough estimates. Second, increasing the completeness at high redshift can come at the expense of introducing more catastrophic spectroscopic redshifts. As we shall show in Sec. 5.3.2, this is a very high price to pay, and can severely increase biases in cosmological parameter constraints.

5.3 Spectroscopic selection matching: culling approach

As can be inferred from the left panel in Fig. 4, spectroscopic failures alter the redshift distribution of the training set significantly, so that one cannot use such a sample to estimate the error distributions of the photometric sample directly. We test two different approaches to correct for the selection effects in the training set.

One approach is to cull the photometric sample to remove all galaxies that are not represented in the training set (the set of high-confidence spectroscopic redshift galaxies). We use a neural network (described in Appendix B) to accomplish this selection matching.

What we want is to be able to classify galaxies in the photometric sample in the same way they were classified in the training set, that is, we need to estimate the cross-correlation strength R statistic for them.

To be more realistic, instead of using R, we map the R values into a new quality parameter Q. The Q parameter is discrete, and roughly matches the more standard quality flags of real surveys (e.g. VVDS, DEEP2). It also has the advantage of having a more limited range than the R statistic, which has no upper limit. The mapping we use is as follows:
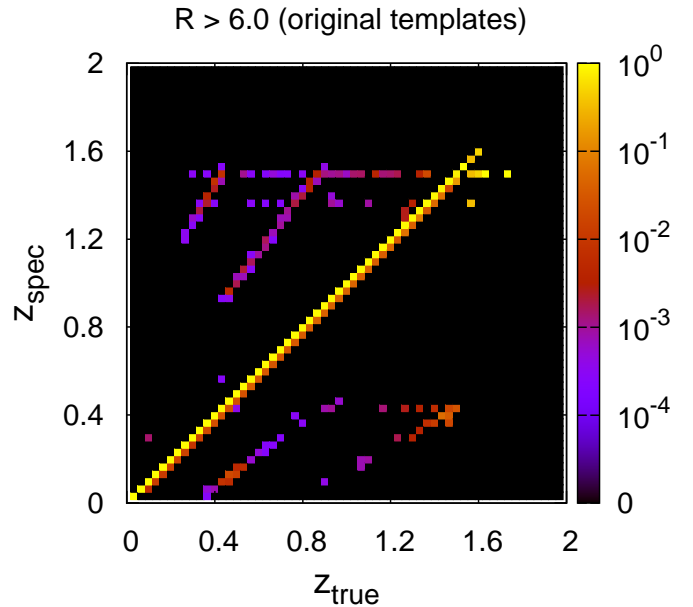
Figure 6. Same as Fig. 5 except for the Original pipeline, where only the 6 original templates were used, and only 4 different values of czguess (no guess, 0.4, 0.8 and 1.2) were used in the rvsao run. Without the 3 additional templates, no strong correlations were found for $z_{\rm spec} > 1.5$, which, in particular, implied that no galaxies were incorrectly assigned $z_{\rm spec} > 1.5$.

$$R \geqslant 6 \iff Q = 4$$
$$5 < R < 6 \iff Q = 3$$
$$4 < R < 5 \iff Q = 2$$
$$3 < R < 4 \iff Q = 1$$
$$0 < R < 3 \iff Q = 0$$

Following standard neural network procedure, we split the spectroscopic sample into two parts (of equal size), the training and validation samples. As described in Appendix B, we use the $griz$ magnitudes as the inputs for the neural network, which then outputs an estimate for Q. For simplicity, we only perform a single

neural net run, though the average of multiple runs is expected to yield best results.

After the neural net run converges, we apply the best-fit function to the complete spectroscopic sample and to the photometric sample to obtain estimates of the Q coefficient, hereafter Q_{est}, for all the galaxies.

For the fiducial simulation - with 16200 secs exposures, 5 combined rvsao runs, the distribution of $Q - Q_{est}$ distribution has dispersion of ~ 0.7. For the 48600 secs exposures scenario, the dispersion is ~ 0.6. For all cases, the mean of the distributions is less than 10^{-5}.

We apply cuts on $Q_{est} = 1.5$, 2.5, and 3.5 to both spectroscopic and photometric samples. With the 16200 sec exposures, the corresponding True SSR for the galaxy samples is 0.996, 0.978 and 0.914, respectively, with a corresponding fraction of objects relative to the total of 0.463, 0.586 and 0.751 in the three cases. For the 48600 sec exposures, we find True SSRs of 0.996, 0,978 and 0.936 respectively, with corresponding fractions of objects retained of 0.655, 0.808 and 0.960.

The next step is to investigate the impact of the selection to the weak lensing analysis. We break up the process into several parts, for clarity:

- If a training set based method is to be used for calculating photo-zs, the first step is to use the training sample with the desired Q_{est} cut to derive photometric redshifts for the matched photometric sample (cf. Sec. 5.3.1). This step may be skipped if a pure template-based algorithm is being used.
- Next, we calculate the WL constraints for the photometric sample selected with the Q_{est} cut and compare that to what we get for the full sample. Constraints degrade both from the reduction in the total number of objects as well as with the shift of the redshift distribution towards lower redshifts (cf. Sec. 5.3.2).
- The next step is to assess the bias resulting from differences in the selection of the spectroscopic and photometric samples as well as the biases due to wrong redshifts. (cf. Sec. 5.3.2).

5.3.1 Photo-z training

We use a neural network photo-z estimator to exemplify the impact of selection matching and wrong redshifts on training-set based photo-z estimation (cf. Sec. 4.2.2). For simplicity, we assume that the photo-zs for the photometric sample should only be calculated for the subset of galaxies surviving the selection cuts of the previous section. In other words, we require that the spectroscopic training sample and the photometric sample have matching selections. We thus define three sets of spectroscopic and photometric samples, specified by the spectroscopic quality cuts on Q_{est} of $Q_{est} > 3.5$, 2.5, or 1.5.

To separate the effects of selection matching from the effect of wrong redshifts, we estimate the photo-zs twice. First, we assume we have the true redshifts for all galaxies passing the Q_{est} cuts, to isolate potential biases due to the spectroscopic selection matching. Then, we perform the photo-z training on the actual spectroscopic redshifts, to gauge the additional impact of wrong redshifts.

Table 1 shows the 1σ photo-z scatter for the samples defined by the Q_{est} cuts. The two z_{true} columns correspond to the scenarios where the true redshifts were used in the training. The scatter is defined as the dispersion in the distribution of $(z_{true} - z_{phot})$ for both the training sample and photometric sample. As expected, the photo-z scatter of the training sample is in excellent agreement with the scatter of the photometric sample, suggesting that both

Photo-z scatter and training set size

Selection	z_{true}		z_{spec}		
	Train	Photo	Train	Photo	Train*
$Q_{est} > 1.5$	0.121	0.121	0.149	0.149	0.214
$Q_{est} > 2.5$	0.098	0.099	0.105	0.106	0.142
$Q_{est} > 3.5$	0.082	0.083	0.081	0.082	0.098

Table 1. Rms scatter of neural network photo-zs for the samples selected by the cuts on estimated z_{spec} quality, $Q_{est} > 1.5$, 2.5, and 3.5. Note that the scatter for the Train*/z_{spec} column is defined as the dispersion in the $z_{spec} - z_{phot}$ distribution, whereas it's defined as the dispersion in the $z_{true} - z_{phot}$ for the other columns.

samples have close to identical photo-z properties and that the selection matching does not introduce any biases. Furthermore, the scatter improves as we apply more stringent cuts on Q_{est}. The decrease in scatter is as expected, since the objects with low Q_{est} are typically the faintest.

The three z_{spec} columns in Table 1 show the more realistic case where the actual spectroscopic redshifts (wrong redshifts included) was used to train the photo-zs. In the $z_{spec}(\mathrm{Train})$ we show the scatter in the training set calculated as the dispersion in the $(z_{true} - z_{phot})$ distribution, which we can see is in excellent agreement with the scatter of the photometric sample shown in the last column. Comparing the dispersion of the $z_{spec}(\mathrm{Photo})$ and $z_{true}(\mathrm{Photo})$ cases, we see that the presence of wrong redshifts degrades the photo-zs of the photometric sample by as much as 20% in the case of the $Q_{est} > 1.5$ cut. The degradation is reduced for the more stringent cuts as the fraction of wrong redshifts is reduced.

In reality, one does not know the true redshifts for the training set, but only the spectroscopic redshifts. Hence, the scatter in the training set photo-zs would be estimated using the spectroscopic redshifts, as the dispersion in the $(z_{spec} - z_{phot})$ distribution. We show this estimate of the scatter in the $z_{spec}(\mathrm{Train}^*)$ column. We see substantially larger values of the scatter compared to the $z_{spec}(\mathrm{Photo})$ column, for all Q_{est} cuts. The point is that the neural network cannot incorporate many of the wrong spectroscopic redshifts into its best-fit solution without a noticeable degradation in the overall fit. As a result, the wrong spectroscopic redshifts show up as catastrophically incorrect redshifts, which we can often remove. We return to this in the next section.

5.3.2 WL constraints and biases

In this section we examine the constraints and biases in the dark energy equation of state w inferred from weak lensing shear-shear correlations. The errors in w are caused by our inability to characterize the photometric redshift error distribution of our sample. In other words, we must know the $P(z_{true}|z_p)$ error matrix for our photometric sample to high accuracy. When we rely on a spectroscopic sample to characterize the error distribution, we are actually estimating $P(z_s|z_p)$, but this distribution differs from the true error matrix $P(z_{true}|z_p)$ because of issues in spectroscopic selection matching and wrong spectroscopic redshifts. We now investigate

how these spectroscopic redshift errors affect the dark energy equation of state measurements.

Table 2 shows the 1σ constraints on w and systematic errors for several different sample selections. The results shown used template-fitting photo-zs described in Sec. 4.2.1. For clarity, we artificially separate the issues due to selection matching from that of the wrong redshifts as follows: we perform the cosmological parameter forecast analysis assuming that all redshifts that passed the Q_{est} selection cut were the correct, true redshifts, thereby explicitly isolating the selection matching systematics. The results are presented under the z_{true} column in Table 2. We can see that biases in w are negligible compared to the statistical constraints, demonstrating that the neural network can accurately match the spectroscopic selection to the photometric sample. The table also shows the fraction of galaxies surviving the selection cuts. For example, for the 16200 secs exposures, we see that the $Q_{est} > 3.5$ cut removes more than half of the sample, which results in nearly a factor of two degradation in the statistical constraints relative to what is achievable with the full sample ($\sigma(w) = 0.055$). The degradation is so severe because most of the objects removed by the cut are at high redshifts.

Next, we examine the impact of wrong redshifts. As the last column of Table 2 shows, wrong redshifts can be devastating to the weak lensing constraints. The bias in w is, perhaps, tolerable only in the $Q_{est} > 3.5$ cases. In the other scenarios one can see that the biases in w are greater than the 1σ constraints even with close to 98% correct redshifts (SSR$_T \simeq 0.98$).

Comparing the 48600 secs and 16200 secs results we see that the magnitude of the biases in w are set entirely by the spectroscopic success rate (SSR$_T$), regardless of the level of completeness. This is another reminder that the emphasis must be on accuracy over completeness.

We investigated the dependence of the results on the photo-z estimator by performing the WL analysis with the neural network photo-zs instead of the template photo-zs. The resulting biases in w are shown in the third column of Table 3. Comparing to the fourth column, where we reproduce the template photo-z biases from Table 2, we see that the magnitude of the bias is very similar for the two photo-z estimators, despite noticeable differences in the photo-z error distributions of both (see e.g. Cunha et al. 2012).

We also tested the possibility of decreasing the biases by culling photo-z outliers. In the presence of wrong spectroscopic redshifts, the culling could remove not only catastrophic photometric redshifts, but perhaps also identify the wrong z_{spec}s. We used the nearest-neighbor error estimator, NNE (Oyaizu et al. 2008a), to cull 10% of the sample selected as the galaxies with largest NNE error, (e_{NNE}). Since the fraction of objects to be culled was fixed, the value of the e_{NNE} cut varied for each catalog and photo-z estimator. The results are presented in the last two columns of Table 3. For simplicity, we did not recalculate the fiducial constraints when deriving the biases for the culled samples; given the qualitative nature of this analysis, this is a reasonable approximation. The NNE cut seems quite effective for the neural network photo-zs, typically reducing the biases by half. When the NNE culling was applied to the template-fitting estimator, the effect was negligible for the $Q_{est} > 3.5$ case, and relatively small for the other cases, suggesting that the NNE is only effective for identifying spectroscopic outliers when a training set based procedure is used. This is by no means obvious since the NNE is very efficient at identifying photo-z outliers even when template-fitting methods are used (Oyaizu et al. 2008a). For comparison, we also tested the effect of applying the same 10% cut using an error estimator from the

Constraints on w (template-fitting photo-zs)					
16200 secs					bias(w)
Selection	Gal. Frac.	SSR$_T$ (%)	$\sigma(w)$	z_{true}	z_{spec}
$Q_{est} > 1.5$	0.75	91.4	0.07	0.004	- 0.52
$Q_{est} > 2.5$	0.59	97.8	0.09	0.002	- 0.13
$Q_{est} > 3.5$	0.46	99.6	0.10	-0.001	- 0.02
48600 secs					
$Q_{est} > 1.5$	0.96	93.6	0.06	0.004	- 0.39
$Q_{est} > 2.5$	0.81	97.8	0.07	0.005	- 0.15
$Q_{est} > 3.5$	0.66	99.6	0.08	0.003	- 0.03

Table 2. Statistical and systematic errors in the dark energy equation of state w for the different Q_{est}-selected samples. The bias results shown used the template-fitting photo-zs. The Gal. Frac. column indicates the fraction of galaxies from the full data set that passed the selection cut, and the SSR$_T$ indicates the fraction of correct redshifts (i.e, fraction for which $|z_{spec} - z_{true}| < 0.01$) in the sample. The true redshifts z_{true} column assumes, artificially, that all galaxies in the spectroscopic sample that passed the Q_{est} cut had perfect spectroscopic redshifts. The z_{spec} column shows the more realistic case where the actual spectroscopic redshifts (including the small fraction of wrong redshifts) were used in the calibration of the photo-z error distributions. Recall that the statistical, marginalized, error in w for perfect redshifts is $\sigma(w) = 0.055$

template-fitting code itself[4]. We find that the biases due to wrong redshifts for the $Q_{est} > 1.5$, 2.5 and 3.5 cases are reduced to -0.41, -0.086 and -0.014, showing that culling using this error estimator is also beneficial. In contrast, note that, in Cunha et al. (2012), we found that culling based on photo-z error estimates had little impact on cosmological biases due to sample variance in calibration sample, despite the effective identification of the photo-z outliers.

Finally, we investigated the dependence of the results on the details of our spectroscopic pipeline, described in Sec. 4.1. We find that our Fiducial pipeline, despite giving the best high redshift completeness, yielded the largest biases in w, shown in the Table 2. The different pipelines yielded consistent trends, and we focus on one particular case, that highlights the importance of the settings. The Original pipeline had a factor of two smaller bias for the $Q_{est} > 3.5$ sample. In the Original setting, recall that only 6 templates were used. As can be seen by comparing the right plot in Fig. 5 with Fig. 6, the 3 additional templates increased the redshift completeness above $z > 1.4$ but resulted in leakage from the high z_{true} bins to low z_{spec} bins. In particular, some galaxies at $z_{true} \sim 1.9$ were assigned z_{spec}s of ~ 0.5 and ~ 0.7. This failure mode was responsible for about 2/3 of the increase in bias in going from the Original to the Fiducial pipeline. The remainder of the difference was due to the fact that the Fiducial pipeline uses `czguess = 1.6` which has the effect of increasing the probability that a galaxy will

---

[4] The error estimate we use is the difference between the `Z_BEST68_HIGH` and `Z_BEST68_LOW` outputs of the *LePhare* code.

Biases in w (Training set photo-zs and NNE)

16200 secs		No NNE Cut		NNE Cut	
Selection	G. Frac.	neural	template	neural	template
$Q_{\mathrm{est}} > 1.5$	0.75	- 0.27	- 0.52	- 0.19	- 0.35
$Q_{\mathrm{est}} > 2.5$	0.59	- 0.13	- 0.13	- 0.06	- 0.11
$Q_{\mathrm{est}} > 3.5$	0.46	- 0.02	- 0.02	- 0.01	- 0.02

Table 3. Biases in the dark energy equation of state w for both the training-set and template-fitting photo-z estimates when the NNE estimator is used to cull outliers in $|z_{\mathrm{phot}} - z_{\mathrm{spec}}|$ space. The 'G. Frac.' column indicates the fraction of galaxies from the full data set that passed the selection cut. Recall that the statistical marginalized errors in w for the three Q_{est} cases are 0.07, 0.09 and 0.10 respectively, as shown in Table 2.

be assigned a high redshift. As a result, the Fiducial pipeline yields z_{spec}s above 1.5 for several galaxies with $z_{\mathrm{true}} < 0.8$.

We conclude that the commonly adopted approach of maximizing the completeness is not recommended because it leads to the increase of the fraction of wrong redshifts which in turn implies worse dark energy parameter biases.

5.4 Spectroscopic selection matching: Weighting approach

In Section 5.3, we matched the selection of the spectroscopic and photometric samples by culling the photometric sample. That is, we selectively removed galaxies from the photometric sample so that it statistically matched, as closely as possible, the spectroscopic sample. In this section we try a more aggressive approach that allows us to keep nearly the full photometric sample. Our technique is to weight galaxies in the spectroscopic sample using the `probwts` method of Lima et al. (2008) and Cunha et al. (2009), so that the statistical properties of these weighted spectroscopic galaxies match those of the photometric sample. For convenience of reference, we briefly describe the `probwts` technique in Appendix C.

We select a training set by picking galaxies from the spectroscopic sample with R above some threshold R_{crit}. We test the reconstruction for several values of R_{crit}. Following standard `probwts` procedure, we remove the (small) part of the photometric sample that is determined to have zero overlap with the spectroscopic sample. This removes at most a few percent of the photometric sample, with negligible impact on the statistical constraints.

Note that, in the first approach, with the neural net, all the spectroscopic sample is used to characterize the spectroscopic selection in observable space. The cosmological analysis is then only performed on the sample that matches the estimated selection. In the second, we only use reliable spectra, which we re-weight to match the full photometric sample. Then, the full photometric sample is used on the cosmological analysis. The first approach is the more conservative one as it throws away photometric data, to keep only the most reliable sample. The second approach is more aggressive as it tries to keep most of the data and only rescale the training set.

As the top plot of Fig. 7 shows, the weights improve the estimate of the overall redshift distribution when true redshifts are used. One can see that the weights roughly fix the broadest discrep-

ancies, but cannot correct sharper features. For example, the dip in the training sample from around $0.4 < z < 0.6$ gets rescaled, but its rough shape persists. What this suggests is that objects in this redshift range occupied the same region of observable space, and the weighting affected them all similarly.

The bottom plot shows the results when the spectroscopic redshifts are used. We see that even a speck of wrong redshifts (2.4% in this case) can have dramatic impact depending on where they are located (cf. bottom plot). Comparing, the bottom plot of Fig. 7 with the middle plot of Fig. 5, we see that the spikes in the Weighted estimated of the redshift distribution at $z \sim 1.5$, 1.4, 0.8, 0.7 and 0.4 all correspond to the regions of concentration of wrong redshifts seen in Fig. 5. However, whereas the spikes below $z = 1$ are not particularly prominent, the spikes around $z = 1.4$ and 1.5 are enormous. There are a couple factors contributing to the problem. As can be inferred from the the left plot in Fig. 2, the completeness drops precipitously above $z > 1.4$. Hence, the few spectroscopic redshifts above $z > 1.4$ typically receive large weights to compensate for the incompleteness. In addition, as shown in the middle plot of Fig. 5, the fraction of correct redshifts for galaxies with $z_{\mathrm{true}} > 1.4$ is very small, and many of these are incorrectly assigned a spectroscopic redshift of $z_{\mathrm{spec}} = 1.4$ or 1.5. The large weights magnify the impact of the wrong redshifts, resulting in the large spikes, and in large bias in the cosmological parameters, as we show in the next section.

5.4.1 Weak lensing constraints and biases with weights

Table 4 shows the 1σ constraints and biases on w when one uses the weights technique to match the spectroscopic selection to the photometric sample. As in Sec. 5.3.2, we separate the analysis into two parts. First, in the z_{true} column, we show only the effect of matching the selection between the spectroscopic and photometric samples. Afterwards, in the z_{spec} column, we use the actual spectroscopic redshifts to show the impact of wrong redshifts.

When one considers only the true redshifts, the weights perform reasonably for all cases. The biases are typically smaller than the statistical errors on w, and the statistical constraints are better than for the culling approach of Sec. 5.3.2 since almost all of the photometric sample was usable for analysis. It is interesting to note that more rigorous cuts (R > 6 and 5) yielded the smallest biases even though the completeness of the spectroscopic sample was smaller than for the R < 4 case. Unfortunately, the z_{spec} column in Table 4 shows that the presence of wrong redshifts severely compromises the weights approach.

Because the wrong redshifts are tightly associated with the regions of high incompleteness, particularly at high redshift, and because the variations in completeness are so sharp, the wrong redshifts received very large weights resulting in large cosmological biases. A major part of the problem is the sharp *change* in completeness with redshift shown on the left plot of Fig. 2. We find that the results for the weights do not improve for the 48600 secs cases because the steep variations in the completeness with redshift become even larger for that case since the increased exposure time did not yield significant increase in completeness above z of 1.4.

In summary, we find that the weights approach needs to be considered with care in the presence of wrong redshifts, and that the more conservative approach of culling using the neural network is the safest. In practice, the weights are often needed to account for other types of incompleteness (see e.g. Cunha et al. 2009), so both approaches should be used in tandem.
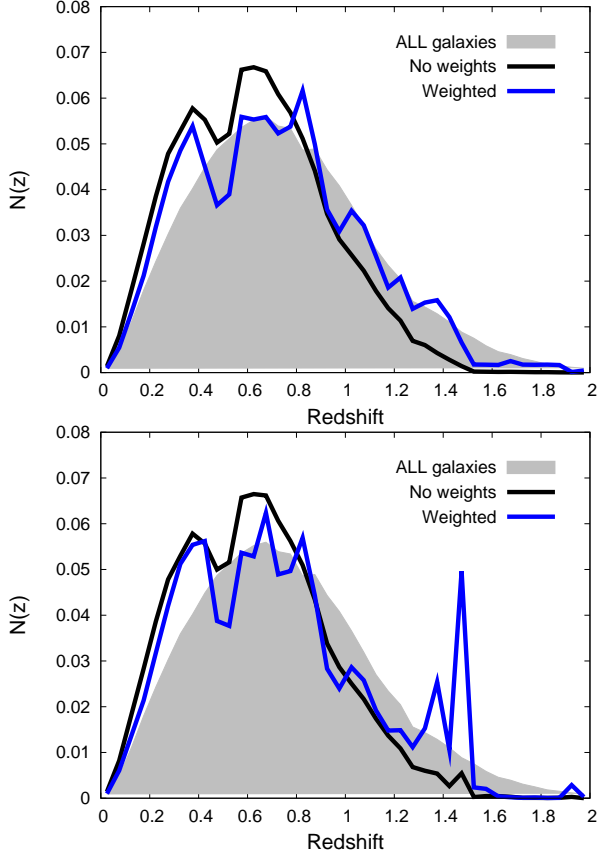
Figure 7. (Top plot) The true redshift distribution of the full photometric sample (shaded gray), of the spectroscopic sample with $R > 5$ with no weights (black line), and with weights (blue - dark gray line). (Bottom plot) Same as above, but showing weighted and unweighted distributions of spectroscopic redshifts. One can see that, because wrong redshifts occupy regions of low completeness in observable space, the weights boost their impact enormously.

Constraints on w (template-fitting photo-zs and weights)

16200 secs					bias(w)
Selection	G. Frac.	SSR_T (%)	$\sigma(w)$	$z_{\rm true}$	$z_{\rm spec}$
$R > 4$	0.73	93.2	0.06	0.070	- 0.7
$R > 5$	0.60	98.6	0.06	0.034	- 0.5
$R > 6$	0.53	99.6	0.06	-0.036	- 0.3

Table 4. Statistical and systematical errors in w when the weights technique for selection matching is used. Results are shown assuming the spectroscopic sample was selected with different cuts of the cross-correlation strength parameter R, described in Sec. 4.1. The bias results shown used the template-fitting photo-zs. The Gal. Frac. column indicates the fraction of galaxies from the *spectroscopic sample* that passed the selection cut, and the SSR_T indicates the fraction of correct redshifts (i.e, fraction for which $|z_{\rm spec} - z_{\rm true}| < 0.01$) in the sample. Essentially all of the photometric sample was used in the analysis.

5.5   Discussion: Robustness of assumptions and results

We now discuss the dependence of our results on the key assumptions and numerical tools used in this work.

• *N-body/photometric simulations*: The success rate statistics are affected by luminosity function and distribution of galaxy types in the simulation. However, the main conclusions of our paper, concerning selection matching and impact of wrong redshifts, should not be affected. We tested the selection matching for a variety of situations (several of which we do not show), including varying atmospheric noise models and spectrograph resolution. For all cases, the matching worked well, incurring no additional bias. In addition, Soumagnac et al. (in preparation) obtain similar results using a very different set of spectro/photometric simulations described in Jouvel et al. (2009).

The distribution of wrong redshifts in ($z_{\rm true}$, $z_{\rm spec}$) space could also change for a different simulation, but the preferred loci where the failures concentrate should not vary appreciably, since they are based on confusion between galaxy or atmospheric spectral lines that do not depend on any details of the simulation. Furthermore, the fact that a small fraction of spectroscopic failures can cause severe biases is not likely to change.

• *Sky noise model:* Our model for sky subtraction is idealized as it assumes a perfect shot-noise model. Sky-subtraction is often not as efficient, and observing conditions vary from the median. In addition, there are issues such as CCD fringing (cf. Sec. 2.3) which are difficult to model. Other effects we did not model include contamination from nearby stars or bright galaxies, and cosmic rays. These other effects, however, are only expected to affect the overall completeness, without galaxy type or redshift dependence.

• *Simulated spectra:* As discussed in Appendix A2, the simulated spectra we use are based on the 5 eigenspectra of kcorrect, which are derived based on about 1600 SDSS main sample galaxies, 400 luminous red galaxies and a photometric sample of several thousands of galaxies imaged in the UV, optical and IR. Is this enough? Yip et al. (2004) showed that a set of 3 eigentemplates were sufficient to describe about 98% of the variance in the 170,000 galaxies in the Strauss et al. (2002) SDSS sample. Additional templates improved coverage very slowly, with a set of 500 eigentemplates needed to account for 99% of the sample variance (cf. Table 1 in that work). Yip et al. (2004) show that the missing variance was due mainly to extreme line-emission galaxies. We roughly confirm this trend for our simulated spectra by looking at the distribution of equivalent widths of the [OII] emission line for our simulated galaxies. We find that our equivalent widths reach at most 30 Å. For comparison, Cooper et al. (2006) find, for the DEEP2 sample, a distribution of [OII] equivalent widths reaching as much as 100 Å.

In addition, Yip et al. (2004) showed that one needs a random subsample of about 10,000 galaxies to obtain convergence for the first 10 eigentemplates. These results suggest the kcorrect basis should be sufficient to characterize all but a few percent of the low-redshift galaxies[5]. However, a few percent of "oddball" galaxies could potentially cause problems for cosmological analysis if they cannot be disentangled from the rest of the sample using colors and if their redshift distribution differs significantly from the rest

---

[5] The Yip et al. (2004) analysis was based on principal component analysis, whereas Blanton & Roweis (2007) used non-negative matrix factorization to determine their respective eigenbasis. Thus, comparison between Blanton & Roweis (2007) and Yip et al. (2004) are only meant as ballpark estimates.

of the sample with similar colors. The problem is expected to become worse at high-redshift. To properly quantify the impact of the outliers, observing campaigns targeted at the spectroscopic failures of existing spectroscopic surveys are crucial.

In some sense, our choice of template library used for deriving spectroscopic redshifts is pessimistic for the high-redshift galaxies: as discussed in Appendix A2, the `kcorrect` templates are based on GALEX colors for the bluer frequencies. Hence, parts of the spectra of high-z objects were simulated using purely photometric data, resulting in excessively featureless spectra in the UV frequencies, which implied lower-than-expected completeness for $z > 1.4$.

• *Spectroscopic redshift pipeline* The `rvsao.xcsao` code uses cross-correlation techniques in Fourier space to derive redshifts from spectra. The disadvantage of this approach relative to a standard χ^2 method is that one does not include any information about the noise. One can disregard certain regions of the spectrum in the analysis, thereby removing at least the most prominent atmospheric lines. We found that the removal of some lines did not increase the completeness of the sample noticeably, and changed the distribution of the wrong redshifts. We leave more extensive tests on the optimal techniques for spectroscopic redshift estimation for a future work.

6 IMPLICATIONS FOR SURVEY DESIGN

Given the findings of this paper and Cunha et al. (2012), what should survey planners do to optimize their spectroscopic surveys?

The first step is obvious: one needs to optimize the allocation of time observing different kinds of galaxies. Specifically, one can use color information to preselect galaxies that will require longer exposure times to obtain accurate redshifts. For example, in Sec. 5.3.2, we saw that tripling the exposure time improved the completeness from 0.46 to 0.66 for the $Q_{est} > 3.5$ cut. If the 20% of the sample that yielded additional redshifts could be known in advance, one would only target this sample for additional observation, which would only require an increase of 40% in the observing time, instead of the naive 200% additional time if the full sample was targeted for follow-up observation. With an optimized observing strategy, one would be able to save precious telescope time and still achieve redshift accuracy that does not degrade the cosmological constraints appreciably. We leave a more detailed analysis for future work.

We showed in this paper that the tolerance for wrong redshifts is extremely low. It is, however, possible to get away with a higher fraction of wrong spectroscopic redshifts by modeling their effects on the cosmological parameters. Then one would need to, in analogy to the photo-z case, fully characterize the spectroscopic error matrix $P(z_{spec}|z_{true})$. However, determining the matrix $P(z_{spec}|z_{true})$ from observations is likely to be very challenging in practice, as in order to control the sample variance of galaxies used for the calibration, one would likely have excessively high requirements on the area of the follow-up (Cunha et al. 2012).

It is also possible that one can use spatial cross-correlations to estimate the spectroscopic error matrix. Since correlations between different redshift bins should be very close to zero, any correlation has to be due to wrong redshifts. Several works have explored this fact for photo-z calibration (Schneider et al. 2006; Erben et al. 2009; Benjamin et al. 2010; Zhang et al. 2010). Schneider et al. (2006), for example, found cross-correlations to work well only in the simplest Gaussian cases. But for spectroscopic failures, the excess correlation signal should be due to a few big outliers, and hence might be more easily detectable.

7 CONCLUSIONS

We investigated the impact of spectroscopic failures on the training and calibration of photometric redshifts, and the consequent impact on the forecasted dark energy parameter constraints from weak gravitational lensing. Our tests were based on N-body/spectrophotometric simulations patterned after the DES and expected spectroscopic follow-up observations loosely patterned after the VVDS survey.

Spectroscopic failures consist of two types of issues: the inability to obtain spectroscopic redshifts for certain galaxies, and incorrect redshifts.

The inability to obtain redshifts introduces incompleteness in the spectroscopic sample — i.e. missing redshifts in some region of parameter space (e.g. at faint magnitudes) represented in the full photometric population of galaxies. This incompleteness must be accounted for before one can use the spectroscopic sample to calibrate photo-zs – i.e characterize the photo-z error matrices, e.g. the $P(z_s|z_p)$, of the sample.

We studied two approaches to account for the incompleteness in the spectroscopic sample. In the first approach, we used an artificial neural network to estimate the spectroscopic selection function for the photometric sample. This selection function was then used to cull the photometric sample so that its statistical properties matched the spectroscopic sample. We found this approach works extremely well, yielding only insignificant bias in the WL constraints using the culled sample (refer to z_{true} column in Table 2). However, the statistical constraints did degrade substantially as, typically, a large fraction of the sample was culled. In the second approach, we accounted for the incompleteness in the spectroscopic sample by applying weights to the galaxies with spectroscopic redshifts, following the approach of Lima et al. (2008), so that the statistical properties of the spectroscopic and photometric samples match. This approach was also successful (cf. z_{true} column in Table 4) — as expected, because most of the photometric sample could be used — yielding tolerable cosmological biases while obtaining the maximum statistical constraints. Overall, we found that the effects of spectroscopic incompleteness are well under control.

Unfortunately, on the other hand, we found that wrong redshifts can significantly degrade cosmological constraints and $> 99\%$ of correct spectroscopic redshifts seems to be needed (cf. SSR_T and z_{spec} columns in Tables 2 and 4). We found the results to be independent of the photo-z estimators used, but somewhat dependent on the settings of the spectroscopic pipeline. In particular, we found that attempts to increase the completeness of the spectroscopic sample during the spectral analysis can result in more catastrophic spectroscopic redshift failures, which will increase cosmological biases.

We tested a couple of approaches to identify wrong spectroscopic redshifts, finding that the NNE error estimator (Oyaizu et al. 2008a) is able to reduce the bias in the measured dark energy equation of state by half while removing only 10% of the photometric sample. Slightly less improvement in the w bias was obtained using the template-fitting error estimator.

In summary, we find that wrong redshifts are by far the main issue affecting calibration of photo-z error distributions with spectroscopic samples. Future follow-up spectroscopic observations of the planned and ongoing wide-area photometric surveys must focus

primarily on the accuracy of the spectroscopic redshifts even if that implies sacrificing the spectroscopic completeness.

APPENDIX A: THE SIMULATIONS

In this section, we describe the construction of the simulations used in our analysis.

A1 N-body/photometric simulations

The simulated galaxy catalog used for the present work was generated using the Adding Density Determined GAlaxies to Lightcone Simulations (ADDGALS) algorithm (Wechsler et al. 2011; Busha et al. 2011a). This algorithm attaches synthetic galaxies to dark matter particles in a lightcone output from a dark matter N-body simulation. The model is designed to match the luminosities, colors, and clustering properties of galaxies.

The simulations used here start with a dark matter lightcone which spans the redshift range from $0 < z < 2$, over one octant of sky (5156 sq. degrees). The lightcone is constructed from three distinct N-body simulations, which range in resolution from a few 10^{10} to a few $10^{11} M_\odot$ particles and box sizes ranging from 1 to 4 Gpc/h. The simulations were run with the LGadget code and modeled a flat ΛCDM cosmology using parameters consistent with WMAP7 results.

The ADDGALS algorithm used to create the galaxy distribution consists of two steps: galaxies based on an input luminosity function are first assigned to particles in the simulated lightcone, after which multi-band photometry is added to each galaxy using a training set of observed galaxies. For the first step, we begin by defining the relation $P(\delta_{dm}|M_r, z)$ — the probability that a galaxy with magnitude M_r a redshift z resides in a region with local density δ_{dm}, defined as the radius of a sphere containing $1.8 \times 10^{13} h^{-1} M_\odot$ of dark matter. This relation can be tuned to reproduce the luminosity-dependent galaxy 2-point function by using a much higher resolution simulation combined with the technique known as subhalo abundance matching. This is an algorithm for populating very high resolution dark matter simulations with galaxies based on halo and subhalo properties that accurately reproduces

properties of the observed galaxy clustering (Conroy et al. 2006; Wetzel & White 2010; Behroozi et al. 2010; Busha et al. 2011b). The relationship $P(\delta_{dm}|M_r, z)$ can be measured directly from the resulting catalog. Once this probability relation has been defined, galaxies are added to the simulation by integrating a (redshift dependent) r-band luminosity function to generate a list of galaxies with magnitudes and redshifts, selecting a δ_{dm} for each galaxy by drawing from the $P(\delta_{dm}|M_r, z)$ distribution, and attaching it to a simulated dark matter particle with the appropriate δ_{dm} and redshift. The advantage of ADDGALS over other commonly used approaches based on the dark matter halos is the ability to produce significantly deeper catalogs using simulations of only modest size. When applied to the present simulation, we populate galaxies as dim as $M_r \approx -14$, compared with the $M_r \approx -21$ completeness limit for a standard halo occupation (HOD) approach.

While the above algorithm accurately reproduces the distribution of satellite galaxies, central objects require explicit information about the mass of their host halos. Thus, for halos with more than 100 particles, we assign central galaxies using the explicit mass-luminosity relation determined from our calibration catalog. We also measure δ_{dm} for each halo, which is used to draw a galaxy from the integrated luminosity function with the appropriate magnitude and density to place at the center.

For the galaxy assignment algorithm, we choose a luminosity function that is similar to the SDSS luminosity function as measured in Blanton et al. (2003), but evolves in such a way as to reproduce the higher redshift observations (e.g., SDSS-Stripe 82, AGES, GAMA, NDWFS and DEEP2). In particular, ϕ_* and M_* are varied as a function of redshift in accordance with the recent results from GAMA (Loveday et al. 2012).

Once the galaxy positions have been assigned, photometric properties are added. We begin with a training set of spectroscopic galaxies and the simulated set of galaxies with r-band magnitudes generated earlier. For each galaxy in both the training set and simulation we measure Δ_5, the distance to the 5th nearest galaxy on the sky in a redshift bin. Each simulated galaxy is then assigned an SED based on drawing a random training-set galaxy with the appropriate magnitude and local density, k-correcting to the appropriate redshift, and projecting onto the desired filters. When doing the color assignment, the likelihood of assigning a red or a blue galaxy is smoothly varied as a function of redshift in order simultaneously reproduce the observed red fraction at low and high redshifts as observed in SDSS and DEEP2.

Differences between the training set and simulated galaxy sample complicate the process of color-assignment. In order to compile a sufficiently large training set, we use a magnitude-limited sample of SDSS spectroscopic galaxies brighter than $m_r = 17.77$ with $z < 0.2$. The simulated sample, on the other hand, is a volume-limited sample, spanning a broader redshift range. When measuring Δ_5 we restrict ourselves to neighbors brighter than $M_r = -19.7$ in the simulation sample, while using all objects in the observational catalog. To mitigate differences in luminosity and redshift, each galaxy is rank ordered according to its density in its redshift bin, and require that objects be in the same percentile bin in each sample rather than having the same the absolute value of Δ_5. This is similar to the method used in Cooper et al. (2008).

The final step for producing a realistic simulated catalog is the application of photometric errors. While the photometric errors generated here are particular to DES, the algorithm can be generalized for any survey. For each galaxy, we add a noise term to the intrinsic galaxy flux, where the noise is drawn from a Gaussian of width

$$\text{noise} = \sqrt{t_e n_p n_s + f_{g,i} t_e} \qquad (A1)$$

where t_e is the exposure time, n_p the number of pixels covered by a galaxy, n_s the flux of the sky in a single detector pixel, and $f_{g,i}$ is the intrinsic flux of the galaxy. Here, galaxies are assumed to have the same angular size, hence n_p is identical for all objects. Application of the above relation to objects from the SDSS catalog shows that it is able to faithfully reproduce the reported errors of the survey.

A2 Creating simulated spectra

We use the `kcorrect v4_1` code (Blanton et al. 2003) to derive simulated spectra. The `kcorrect` code includes a set of 5 eigenspectra derived using a non-negative matrix factorization (NMF) technique (Blanton & Roweis 2007). To derive the eigenspectra, the authors start out with a basis of 450 star formation history templates from Bruzual & Charlot (2003) as well as 35 templates from Kewley et al. (2001). The method uses this basis to derive the nonnegative linear combination of templates that best described the observations. In this case, the observations consist of a sample of several thousand photometrically and/or spectroscopically observed galaxies, from the far UV to the near IR (Blanton & Roweis 2007). The spectroscopic part of the training data consisted of 400 SDSS luminous red galaxies (LRGs) with $0.15 < z < 0.5$ (Eisenstein & other 2001) and 1600 SDSS main sample galaxies with $0.0001 < z < 0.4$ (Strauss et al. 2002), with both sets of data observed in the range $3800\text{Å} < \lambda < 9000\text{Å}$.

We use the `kcorrect` subroutine to convert the true redshift and error-free magnitudes of a simulated galaxy from our photometric simulation into a best-fitting spectral energy distribution (SED). The SED is characterized by the coefficients of the 5 eigentemplates, and are output as the variable `coeffs`. The `coeffs` are then passed into the subroutine `k_reconstruct_spec`, which produces a simulated spectrum with a resolution, in units of velocity dispersion, of 300 km/s.

We pattern our mock survey loosely on the VIMOS-VLT Deep Survey (VVDS; Le Fèvre et al. 2005). The characteristics of the instrument that we assume are: collecting area of 16π m^2, aperture of 5×0.5 arcsecs^2. For simplicity, we assume a constant resolution and a dispersion of $\Delta\lambda = 7.14/\text{pixel}$ over the entire spectrograph range of $5500 - 9500\text{Å}$. Comparing the spectrograph window of $5500 - 9500\text{Å}$ to the spectroscopic coverage of the training set used to create the simulated spectra, we see that for objects below redshift of 0.05, there is no spectroscopic representation of the training set galaxies in the range $9000 - 9500\text{Å}$. More problematic is the fact that the spectroscopic training set has wavelength coverage starting at 3800Å, and only goes to $z = 0.4$. As a result, for galaxies at about $z > 1.0$, the blue side of the simulated spectra are based solely on photometric data. Considering that most of the SDSS main sample is below redshift of 0.2, the simulated spectra should begin to lose resolution in the blue-end for $z > 0.73$. These limitations in the simulated spectra result in higher-than-expected incompleteness above $z = 1.4$, but do not affect the overall conclusions.

We use a Palomar sky extinction model (courtesy of B. Oke and J. Gunn) with 1.3 airmasses and altitude of 2635 meters to calculate the atmospheric transmission fraction (the solid black line in the bottom panel of Fig. A1). The instrument transmission is based

on the VIMOS instrument transmission function[6] and is shown as the dashed red line in the bottom panel of Fig. A1. The total transmission is the product of the atmospheric and instrumental transmissions. We assume 16200 secs exposures for the fiducial observation strategy and also investigate a scenario with 48600 secs exposures.

We add atmospheric emission based on the sky spectrum[7] shown at the top panel of Fig. A1. The total noise is given by the rms sum of the atmospheric noise, shot-noise from the galaxy spectrum itself and readout noise per pixel, which we take to be a constant 5 photons. In reality, we only simulate the sky-subtracted spectrum, as follows. First, we convert the different spectra into photon counts for each pixel. We then assume the atmospheric and galaxy noise follow a Poisson distribution, so that the uncertainty in the produced noise is the square-root of the number of photons emitted. The readout noise is taken to be Gaussian. We calculate the total noise, N as

$$N = \sqrt{n_{\text{atm}} + n_{\text{gal}} + n_{\text{read}}^2} \qquad (A2)$$

where n_{atm}, n_{gal}, and n_{read} are the number of photons from the atmosphere, the galaxy and the readout noise, respectively. The expected signal is simply the total number of photons from the galaxy. The expectation value of the error in the flux, δF is then given by

$$\delta F = F \frac{N}{S} \qquad (A3)$$

To obtain the sky-subtracted galaxy spectrum we, at each pixel, sample from a Gaussian distribution with mean given by the flux and width given by the error in the flux δF.

APPENDIX B: ARTIFICIAL NEURAL NETWORKS

We use an Artificial Neural Network (ANN) method to both estimate the spectroscopic redshift quality and photometric redshifts, using an implementation based on (Collister & Lahav 2004; Oyaizu et al. 2008b) Despite the fancy name, an ANN is simply a function which relates redshifts (or any quantity we wish to estimate) to photometric observables. The training set is used to determine the best-fit value for the free parameters of the ANN. The best-fit parameters are found by minimizing the overall scatter of the photo-zs determined for the training set galaxies. The ANN configurations are not unique in the sense that different sets of parameters can result in the same overall scatter. The best-fit parameters found after minimizing the scatter depend on where in parameter space the optimization run begins. Hereafter we refer to an ANN function using a given set of best-fit parameters as a neural network solution.

The technical details are as follows. We use a particular type of ANN called a Feed Forward Multilayer Perceptron (FFMP), which consists of several nodes arranged in layers through which signals propagate sequentially. The first layer, called the input layer, receives the input photometric observables (magnitudes, colors, etc.). The next layers, denoted hidden layers, propagate signals until the output layer, whose outputs are the desired quantities, in this case the photo-z estimate or the redshift quality Q estimate. Following

---

[6] http://www.eso.org/observing/etc/bin/gen/form?
INS.NAME=VIMOS+INS.MODE=SPECTRO
[7] Sky spectrum obtained from http://www.gemini.edu/sciops/
ObsProcess/obsConstraints/atm-models/skybg_50\
_10.dat
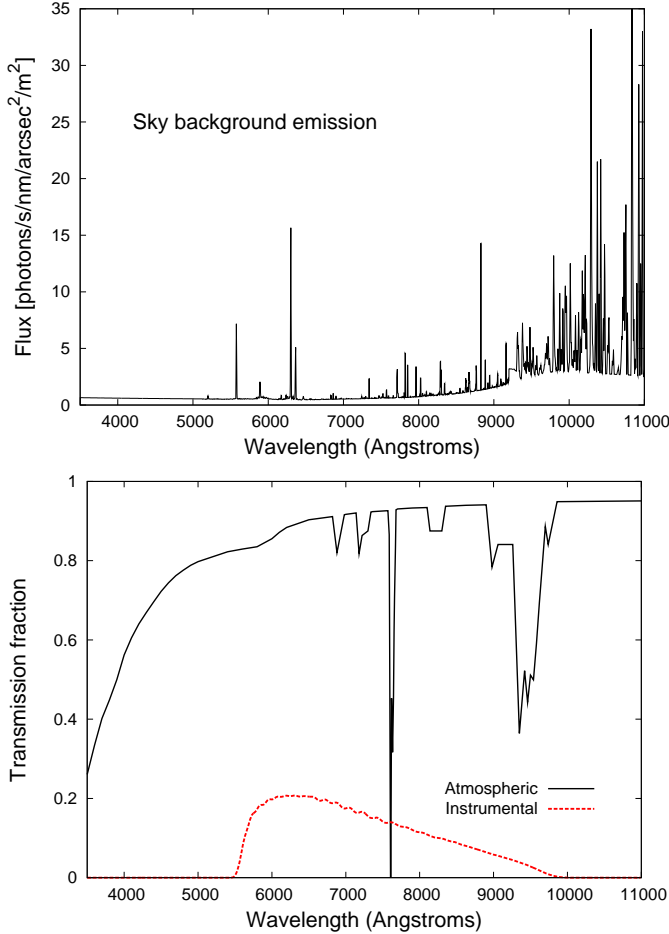
Figure A1. Top panel: Atmospheric emission in units of photons/s/nm/m^2/arcsec^2. Bottom panel: Atmospheric and instrumental transmission fractions, i.e fraction of photons that reach the focal plane, used in our simulation. The total transmission function is given by the product of the two transmissions.

the notation of Collister & Lahav (2004), we denote a network with k layers and N_i nodes in the ith layer as $N_1 : N_2 : ... : N_k$.

A given node can be specified by the layer it belongs to and the position it occupies in the layer. Consider a node in layer i and position α with $\alpha = 1, 2, ..., N_i$. This node, denoted $P_{i\alpha}$, receives a total input $I_{i\alpha}$ and fires an output $O_{i\alpha}$ given by

$$O_{i\alpha} = F(I_{i\alpha}), \tag{B1}$$

where $F(x)$ is the activation function. The photometric observables are the inputs $I_{1\alpha}$ to the first layer nodes, which produce outputs $O_{1\alpha}$. The outputs $O_{i\alpha}$ in layer i are propagated to nodes in the next layer $(i + 1)$, denoted $P_{(i+1)\beta}$, with $\beta = 1, 2, ..N_{i+1}$. The total input $I_{(i+1)\beta}$ is a weighted sum of the outputs $O_{i\alpha}$

$$I_{(i+1)\beta} = \sum_{\alpha=1}^{N_i} w_{i\alpha\beta} O_{i\alpha}, \tag{B2}$$

where $w_{i\alpha\beta}$ is the weight that connects nodes $P_{i\alpha}$ and $P_{(i+1)\beta}$. Iterating the process in layer $i + 1$, signals propagate from hidden layer to hidden layer until the output layer. In our implementation, we use a network configuration $N_m : 10 : 10 : 10 : 1$, which receives N_m magnitudes and outputs a photo-z or a spectroscopic redshift quality. We use hyperbolic tangent activation functions in the hidden layers and a linear activation function for the output layer.

APPENDIX C: PROBWTS

In this subsection, we briefly review the weighting method[8] of Lima et al. (2008) and Cunha et al. (2009). We define the weight, w, of a galaxy in the spectroscopic training set as the normalized ratio of the density of galaxies in the photometric sample to the density of training-set galaxies around the given galaxy. These densities are calculated in a local neighborhood in the space of photometric observables, e.g. multi-band magnitudes. In this case, the DES *griz* magnitudes are our observables. The hypervolume used to estimate the density is set here to be the Euclidean distance of the galaxy to its Nth nearest-neighbor in the training set. We set $N = 2$, to derive the most localized estimates possible.

The weights can be used to estimate the redshift distribution of the photometric sample using

$$N(z)_{\text{wei}} = \sum_{\beta=1}^{N_{\text{T,tot}}} w_\beta N(z_1 < z_\beta < z_2)_{\text{T}}, \tag{C1}$$

where the weighted sum is over all galaxies in the training set. Lima et al. (2008) and Cunha et al. (2009) show that this provides a nearly unbiased estimate of the redshift distribution of the photometric sample, $N(z)_{\text{P}}$, provided the differences in the selection of the training and photometric samples are solely done in the observable quantities used to calculate the weights.

REFERENCES

Abdalla F.B., Banerji M., Lahav O., Rashkov V., 2011, Mon. Not. R. Astron. Soc., 417, 1891

Abdalla F.B. et al., 2008, Mon. Not. Roy. Astron. Soc., 387, 969

Abrahamse A., Knox L., Schmidt S., Thorman P., Tyson J.A., Zhan H., 2011, Astrophys. J., 734, 36

Amara A., Refregier A., 2007, Mon. Not. Roy. Astron. Soc., 381, 1018

Arnouts S., Cristiani S., Moscardini L., Matarrese S., Lucchin F., Fontana A., Giallongo E., 1999, Mon. Not. R. Astron. Soc., 310, 540

Behroozi P.S., Conroy C., Wechsler R.H., 2010, Astrophys. J., 717, 379

Benjamin J., Van Waerbeke L., Menard B., Kilbinger M., 2010, Mon.Not.Roy.Astron.Soc., 408, 1168

Bernstein G., Huterer D., 2010, Mon. Not. R. Astron. Soc., 401, 1399

Blanton M.R., Roweis S., 2007, Astro. Journal, 133, 734

Blanton M.R. et al., 2003, Astrophys. J., 592, 819

Bordoloi R., Lilly S., Amara A., Oesch P., Bardelli S. et al., 2012

Bordoloi R., Lilly S.J., Amara A., 2010, Mon. Not. R. Astron. Soc., 406, 881

Bruzual G., Charlot S., 2003, Mon. Not. R. Astron. Soc., 344, 1000

Busha M., Wechsler R. et al., 2011a, in preparation

Busha M.T., Wechsler R.H., Behroozi P.S., Gerke B.F., Klypin A.A., Primack J.R., 2011b, ApJ, in press

Coe D., Benítez N., Sánchez S.F., Jee M., Bouwens R., Ford H., 2006, Astro. Journal, 132, 926

Coleman G.D., Wu C.C., Weedman D.W., 1980, Astrophys. J. Supp., 43, 393

Collister A.A., Lahav O., 2004, Proc. Astron. Soc. Pac., 116, 345

Conroy C., Wechsler R.H., Kravtsov A.V., 2006, Astrophys. J., 647, 201

Cooper M.C., Tremonti C.A., Newman J.A., Zabludoff A.I., 2008, Mon. Not. R. Astron. Soc., 390, 245

Cooper M.C. et al., 2006, Mon. Not. R. Astron. Soc., 370, 198

Cunha C.E., Huterer D., Busha M.T., Wechsler R.H., 2012, Mon. Not. R. Astron. Soc., 423, 909

Cunha C.E., Lima M., Oyaizu H., Frieman J., Lin H., 2009, Mon. Not. R. Astron. Soc., 396, 2379

Eisenstein D.J., other, 2001, Astro. Journal, 122, 2267

Erben T. et al., 2009, A&A, 493, 1197

Feldmann R. et al., 2006, Mon. Not. R. Astron. Soc., 372, 565

Hearin A.P., Zentner A.R., Ma Z., Huterer D., 2010, Astrophys. J., 720, 1351

Hildebrandt H. et al., 2010, A&A, 523, A31

Huterer D., Linder E.V., 2007, Phys. Rev., D75, 023519

Huterer D., Takada M., Bernstein G., Jain B., 2006, Mon. Not. R. Astron. Soc., 366, 101

Huterer D., Turner M.S., 2001, Phys. Rev., D64, 123527

Ilbert O. et al., 2006, A&A, 457, 841

Jouvel S. et al., 2009, A&A, 504, 359

Kewley L.J., Dopita M.A., Sutherland R.S., Heisler C.A., Trevena J., 2001, Astrophys. J., 556, 121

Kitching T.D., Taylor A.N., Heavens A.F., 2008, Mon. Not. Roy. Astron. Soc., 389

Knox L., Scoccimarro R., Dodelson S., 1998, Phys. Rev. Lett., 81, 2004

Kurtz M.J., Mink D.J., 1998, Proc. Astron. Soc. Pac., 110, 934

Le Fèvre O. et al., 2005, A&A, 439, 845

Lima M., Cunha C.E., Oyaizu H., Frieman J., Lin H., Sheldon E.S., 2008, Mon. Not. R. Astron. Soc., 390, 118

Loveday J. et al., 2012, Mon. Not. R. Astron. Soc., 420, 1239

Ma Z., Bernstein G., 2008, Astrophys. J., 682, 39

Ma Z., Hu W., Huterer D., 2006, Astrophys. J., 636, 21

Nakajima R., Mandelbaum R., Seljak U., Cohn J.D., Reyes R., Cool R., 2012, Mon. Not. R. Astron. Soc., 420, 3240

Newman J.A. et al., 2012, preprint (arXiv:1203.3192)

Oyaizu H., Lima M., Cunha C.E., Lin H., Frieman J., 2008a, Astrophys. J., 689, 709

Oyaizu H., Lima M., Cunha C.E., Lin H., Frieman J., Sheldon E.S., 2008b, Astrophys. J., 674, 768

Schneider M., Knox L., Zhan H., Connolly A., 2006, Astrophys. J., 651, 14

Strauss M.A. et al., 2002, Astro. Journal, 124, 1810

Tonry J., Davis M., 1979, Astro. Journal, 84, 1511

Wechsler R.H., T. B.M. et al., 2011, in preparation

Wetzel A.R., White M., 2010, Mon. Not. R. Astron. Soc., 403, 1072

Yip C.W. et al., 2004, Astro. Journal, 128, 585

York D.G. et al., 2000, Astro. Journal, 120, 1579

Zhang P., Pen U.L., Bernstein G., 2010, Mon. Not. R. Astron. Soc., 405, 359